Transient multi-physics analysis of a magnetorheological shock absorber with inverse Jiles-Atherton hysteresis model

Jiajia Zheng[1], Yancheng Li[3], Zhaochun Li[1,2] and Jiong Wang[1]

[1] School of Mechanical Engineering, Nanjing University of Science and Technology, Nanjing, China

[2]School of Mechanical Engineering, Nanjing Forestry University, Nanjing, China

[3]School of Civil and Environmental Engineering, University of Technology, Sydney, Australia

Abstract

This paper presents multi-physics modeling of a MR absorber considering the magnetic hysteresis to capture the nonlinear relationship between the applied current and the generated force under impact loading. The magnetic field, temperature field and fluid dynamics are represented by the Maxwell equations, Conjugate heat transfer equations and Navier-Stokes equations. These fields are coupled through the apparent viscosity and the magnetic force, both of which in turn depend on the magnetic flux density and the temperature. Based on a parametric study, an inverse Jiles-Atherton hysteresis model is used and implemented to the magnetic field simulation. The temperature rise of MR fluid in the annular gap caused by core loss (i.e. eddy current loss and hysteresis loss) and fluid motion are computed to investigate the performance of current-force behavior. A group of impulsive tests were performed for the manufactured MR absorber with step exciting currents. The numerical and experimental results showed good agreement, which validates the effectiveness of the proposed multi-physics FEA model.

KEY WORDS

MR shock absorber; multi-physics; inverse Jiles-Atherton model; transient; impact loading;

1. Introduction

So far the major drawback of the magnetorheological (MR) absorber in the semi-active control applications lies in the non-linear and hysteresis characteristics [1]. Therefore, the accurate modelling of the MR damper becomes a vital task to advance its applications. The modelling techniques for the MR damper behavior can be grouped into two categories: phenomenological modelling and physical modelling [2]. Phenomenological modelling itself generally can be grouped into two kinds: parametric modelling and non-parametric modelling. For the parametric modeling, the parameters have physical meanings such as spring, viscous damper, friction elements etc. Several parametric models have been proposed in the literature, including the hysteretic Bingham plastic model [3], the Bouc-Wen model [3,35], the non-linear viscoelastic model [4], the hysteretic Bi-viscous model [5] and Dahl model [6]. On the other hand, the applications of non-parametric models such as the polynomial model [7], the generalized

Email: znjust_cn163.com

sigmoid function model [8], neural networks [9, 10], and neuro-fuzzy [11] are limited due to the lacking of physical conceptions. In contrast to phenomenological models, the physical models [12-14] which can numerically or analytically compute the damping force directly using the geometrical parameters of the MR damper and the material characteristics of the MR fluids.

However, all of the above-mentioned models focus on the non-linear force-displacement and hysteretic force-velocity characteristics, the response of current-force was rarely paid attention to. In fact, the non-linear effects due to the inherent hysteresis of ferro-magnetic material in the process of magnetic field excitation considerably affect the performance of the MR actuators [15]. At the moment the factors that affect the delay phenomenon of current and force can be concluded as: fluid compressibility, ferro-magnetic material hysteresis and eddy current. It is noted that the influence of fluid compressibility on the delay phenomenon can be ignored under high velocity [16]. Therefore, the magnetic hysteresis of the ferro-magnetic material and induced eddy current are the major factors in the nonlinearity of the current-force curves of MR absorber. In this regard, a hysteresis model is required to capture the nonlinear characteristics of the magnetic circuits and incorporate the model into a control algorithm.

Studies on implementing the ferro-magnetic hysteresis model into the MR dampers are rather limited in the literatures. An *et al* [15] implemented the Hodgdon's model into a disc-type MR brake and the results show that the proposed model characterized the hysteresis behavior of the major loop. Jedryczka *et al* [17] applied Jile-Atherton hysteresis model into a MR-clutch and successfully estimate the output torque. Instead of hysteresis modelling techniques, Erol *et al* [18] embedded a Hall-effect sensor in the flux path to measure the magnetic flux across the MR fluid. Although all those work have been useful in modelling ferro-magnetic hysteresis, it is not straight forward to understand the certain aspects of their behaviors. Some phenomena cannot be well explained by the above hysteresis models, such as temperature rise due to energy dissipation, fluid flow and pressure drop within the damper, To address these issues, MR absorbers can be further analyzed using a multi-physics FEA model which is in its capacity to model complex interacting fields such as electromagnetism, heat transfer and fluid dynamics [19]. This state-of-the-art in FEM modelling enables us to understand the internal hysteresis behavior of MR damper prior to experimental work.

The main contribution of the work is the development of a multi-physics FEA model based on the inverse Jiles-Atherton hysteresis model for a MR absorber under impact loading. The net magnetic flux density in the fluid gap was calculated taking the eddy current into account. Based on a parametric study, an inverse Jiles-Atherton hysteresis model is used and implemented into the magnetic field simulation. By applying an alternating exciting current, the temperature rise of MR fluid in the annular gap caused by core loss (i.e. eddy current loss and hysteresis loss) and fluid motion are calculated to investigate the performance of current-force behavior. Furthermore, taking the magnetic hysteresis and thermal effect into consideration, a transient multi-physics simulation is performed to understand the dynamic response of current-force characteristics. Finally, a group of impulsive tests were performed for the manufactured MR absorber with step constant exciting densities and the results between numerical

and experimental were compared and discussed.

2. Geometry of multi-coil MR absorber

In view of a MR absorber, the basic assembly components involve the cylinder and control valve: the former is usually filled with MRFs and separated by a moveable piston and the latter is employed to produce the damping effect under the controllable magnetic fields using electromagnetics [20]. To reduce the size, a typical structure of mono-tube MR absorber was designed with the control valve assembled in the piston as shown in figure 1. During the piston movement, MR fluids in the cylinder pass from compression chamber to extension chamber through the control valve, which causes the damping force proportional to the controllable magnetic field by altering its apparent viscosity. The control valve was designed with four-stage magnetic coils to enlarge the maximum damping force. The guide head which is connected with the piston head aims to avoid the eccentricity during the reciprocation of the MR shock absorber. The test points (A-E) located along the centerline of the working gap are employed to monitor the local magnetic flux densities as shown in figure 8. The main geometric parameters of the four-coil MR damper are given in table 1 based on the previous work [32]. The assembly components of the manufactured MR absorber are shown in Figure 2. Please note that the full stroke of the designed MR absorber is 650[mm] and the singular damping movement is less than 600 milliseconds under regular impact loading [21].

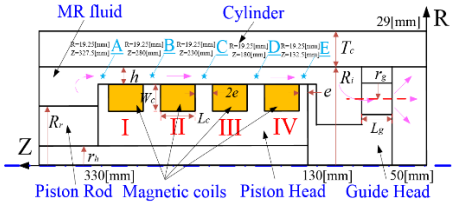

Fig 1. Schematic diagram of multi-coil MR absorber

Fig 2. Photograph of manufactured MR absorber

Table 1 Design parameters of MR absorber

Piston head radius (R_i)	18.5[mm]	Gap size (h)	1.5[mm]
Bobbin height (W_c)	8[mm]	Rod radius (R_r)	14[mm]
Cylinder thickness (T_c)	9[mm]	Hole length of guide head (L_g)	10[mm]
Hole radius of guide head (r_g)	2[mm]	Active length (e)	5[mm]
Hole radius of piston rod (r_h)	3[mm]	Bobbin length (L_c)	40[mm]

3. Multi-physics finite element model

To better understand certain aspects of their behaviors, such as temperature rise, magnetic flux formation, internal pressure rise and their interactions with each other, multi-physics modeling of interacting fields is presented in the following sections. The materials used in this research have the nominal properties shown in table 4.

3.1 Magnetic field

3.1.1 Eddy current

Previous numerical integration strategy proposed for the coupled problem was first to solve the set of field equations of the magnetic field, and afterwards apply these results into the fluid problem [22, 23]. It is based on the assumption that the magnetic is invariant in time, which is true when the applied current is constant. However, magneto-rheological devices rarely operates under steady-state conditions, it is important to make the fluid dynamics and magnetic field models interact synchronously subjected to transient operations of electromagnets with varying current intensity. With the magnetic flux $\emptyset$ changing in time, the piston (ferro-magnetic material) generates an electromotive force Θ_{inv} which is the time derivative of the magnetic flux, i.e.

$$\Theta_{inv} = -N\frac{d\emptyset}{dt} \quad (1)$$

where N is the turns of copper wire .

The induced electromotive force (EMF) generates eddy currents in the piston and external casing of the MR absorber. An eddy current creates a magnetic field that opposes the target magnetic field and thus the net magnetic flux is reduced, which is identified as the principal cause of the slower force increase or decrease than that of the input current as the MR damper switches between its passive and active modes [16]. To better understand the influence of the eddy current on the resultant magnetic flux density, a finite element simulation concerning variable magnetic fields was performed based on the COMSOL Multi-physics software. The dependent variable in this physics is the azimuthal component of the magnetic vector potential A_φ , which in frequency domain obeys the relation:

$$(j\omega\sigma - \omega^2\varepsilon)A_\varphi + \nabla \times \left(\mu^{-1}\nabla \times A_\varphi\right) = J_\varphi \quad (2)$$

$$\vartheta = \sqrt{\frac{2\rho}{\omega\mu_0\mu_r}} \quad (3)$$

where ω is the angular frequency $(2\pi f)$, σ is the electric conductivity, μ is the magnetic permeability, ε is the electric permittivity, and J_φ denotes the current density due to an external source; ρ is the density and ϑ is a constant called the skin depth that is defined as the depth below the surface of the conductor at which the current density decays to about 0.37 of the current density on the surface.

The eddy current only occurs within a changing magnetic field and is zero when the magnetic field reaches a steady state. Each of the four magnetic coils has 500 turns of American wire gauge (AWG) #21 copper wires and is applied with an input current of 2[A]. Two adjacent fluxes travel in the opposite directions, but interact constructively along the shared flux paths. As explained before, the eddy current generates opposite magnetic field, reducing the value of the net magnetic field. For instance, the average magnetic flux density in the fluid gap of the MR damper obtains 0.77 [T] by applying each of the magnetic coil with 2[A] DC current. However, with the frequency of the applied alternating current (AC) varying from 2.5 to 10[Hz], the average net magnetic flux density on the fluid region reduces to 0.71[T] as shown in figure 3. One possibility to reduce the eddy current by simple geometric modification has been deemed ineffective [16]. However, regardless of eddy current, overshooting current intensity steps may be an option to achieve the desired net magnetic flux density in the fluid region. The ways to eliminate the eddy current remain open to further study.

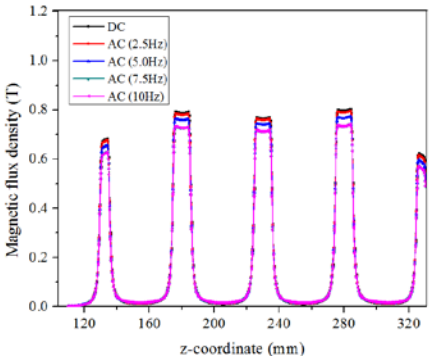

Fig 3. Magnetic flux density in the fluid gap

3.1.2 Inverse Jiles-Atherton hysteresis model

When an external magnetic field is applied to a ferro-magnetic material such as steel, the atomic dipoles align themselves with it. Even when the field is removed, part of the alignment is still retained and must be driven back to zero by a field in the opposite direction. If an alternating exciting current $i = I_{max}\sin(\omega t)$ is applied to a ferro-magnetic material, a hysteresis loop is traced out by its magnetization $\boldsymbol{M}$ as shown in figure 4. Let us assume that the ferro-magnetic material has no initial residual field when the coil is excited by $i = I_{max}\sin(\omega t)$. In the interval $0 < \omega t <$

$\pi/2$, magnetic flux density $\boldsymbol{B}$ rises along the path OGP and the operating point at P corresponds to $+I_{max}$ or $+H_{max}$. For the interval $\pi/2 < \omega t < \pi$, operating moves along the path PRT and the exciting current is zero at point T. Next, the sinusoidal current i starts increasing in the opposite direction and the operating point moves along TSEQ. It should be noted that the value OS which is called the coercivity of the material is necessary to bring the residual field back to zero at point S. At the end of the interval $\pi < \omega t < 3\pi/2$, exciting current i reaches $-I_{max}$ or $-H_{max}$. In the next interval $3\pi/2 < \omega t < 2\pi$, exciting current i changes from $-I_{max}$ to zero and operating point moves from Q to M along the path F. After this a new cycle of the current variation begins and the operating point moves along the path MNKP instead of OGP. During the hysteresis process, the intervals are experiencing energy absorbing and returning. Thus the total area enclosed by the B-H loop is the measure of the hysteresis loss per unit volume per unit cycle and is $P_h = f \oint HdB \ [W/m^3]$. The hysteresis loss can also be expressed empirically as shown in equation (11).

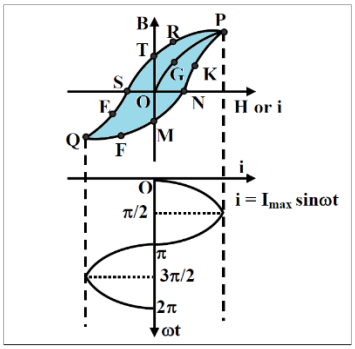

Fig 4. B-H loop with sinusoidal current

To fully capture the phenomenon of the dynamic hysteresis loss, a precise modeling of the ferro-magnetic materials is a prerequisite. Among the existing hysteresis models, the Jiles-Atherton model is widely used due to its relative simplicity and ease in numerical implementation [24]. In the original Jiles-Atherton model [25, 26], the magnetic hysteresis is characterized by the reversible component M_{rev} and its irreversible component M_{irr} and energy losses relative to the equilibrium anhysteretic magnetization M_{an}. Using this method, the magnetization $\boldsymbol{M}$ is commonly obtained from the magnetic field $\boldsymbol{H}$. To directly obtain the magnetization $\boldsymbol{M}$ and the magnetic field $\boldsymbol{H}$ from the magnetic induction $\boldsymbol{B}$, an inverse Jiles-Atherton model [27] is used and its numerical procedure is shown in Figure 5.

To implement this inverse Jiles-Atherton model in field calculation, the most obvious way based on μ_0 and $\boldsymbol{M}$ formulation is adopted by substituting the vector equation ② of figure 5 (b) into the Ampere's law. Using the axisymmetric 2-D dimensional magnetic vector potential A_φ, the field equation is given by

$$\frac{1}{\mu_0} \cdot \nabla \times A_\varphi(t+\Delta t) = J_\varphi(t+\Delta t) + \nabla \times M(t+\Delta t) \quad (4)$$

where $A_\varphi(t+\Delta t)$, $J_\varphi(t+\Delta t)$ and $\boldsymbol{M}(t+\Delta t)$ are the φ-component magnetic vector potential, the φ-component current density and the magnetization vectors at time $(t+\Delta t)$ respectively. The finite element method is used to solve the equation (4) and $B(t+\Delta t)$ is evaluated at each iteration according to the adopted formulation.

3.1.3 Parametric study of inverse J-A parameters

The inverse J-A model is very useful for simulating hysteresis curves of the ferro-magnetic materials. The main objective of the simulation using inverse J-A model is to understand the influence of magnetic hysteresis on the dynamic performance of MR absorber, especially in particular time-urgent situations (i.e. impact loading). To better fit over the entire range of the hysteresis loop, a parametric study of the J-A parameters (a, α, c, k) has been performed as follows.

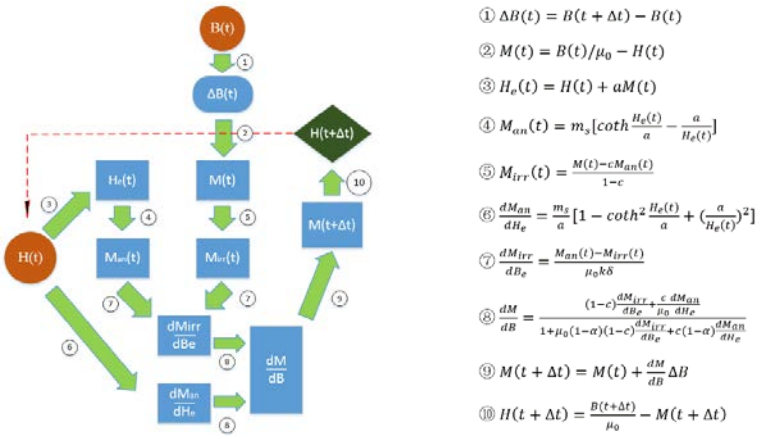

(a) (b)

Fig 5. Inverse Jiles-Atherton model (a): Numerical procedure to calculate M and H from B (b): Relevant formulas (a, α, c, k and m_s are parameters which are determined from the measured hysteresis characteristics, δ is the directional parameter and is +1 for $dH/dt > 0$ and -1 for $dH/dt < 0$)

Figure 6(a) shows the effect of parameter 'a' on the shape of the B-H hysteresis curve. It can be seen that the parameter 'a' is inversely proportional to the magnetic moment of average domain, in other words, the slope of the curve in the reversible region becomes steep as the parameter 'a' is low. As shown in figure 6(b), the parameter 'α' has little effects on the shape of the curve except the residual magnetism M_r, which increases as the parameter 'α' increases. The parameter 'c' known as the reversible movement of the domain wall, has large effects on the shape of the hysteresis curve, which indicates the reversible effect dominated at low fields (figure 6(c)). The coercivity is determined by the amount of spinning and hence by the parameter 'k' in the model. As shown in figure 6(d), with the parameter 'k' increasing, the slope of the hysteresis curve decreases meanwhile the coercivity H_c increases significantly. For the saturation magnetization M_s, it is often chosen from the experimental results.

To test the inverse Jiles-Atherton model, the alternating current (AC) i is applied on each electromagnetic coil by

$$i = I_{max}\sin(2\pi f t)$$

$$I_{max} = \begin{cases} 0.5A & 0 < t < 0.2[s] \\ 1.0A & 0.2[s] \le t < 0.4[s] \\ 1.5A & 0.4[s] \le t < 0.6[s] \end{cases} \quad (5)$$

Figure 7 shows the simulated magnetic loop at the operation frequency of $5[Hz]$. One can observe that the hysteresis loop becomes larger with the increase of exciting current as expected. Furthermore, the hysteresis loop cannot be repeatable due to the existence of hysteresis characteristics. Further phenomenon can be found in figure 8 which show that the magnetic field density generated in the fluid gap lags behind the alternating current. Please note that the test points (A-E) locate in the MR fluid gap upon the five ferro-magnetic poles as shown in figure 1. Therefore, the hysteresis phenomenon of ferro-magnetic material is important to be taken into account for capturing precise nonlinear characteristics of both MR fluids and the magnetic circuit in real-time.

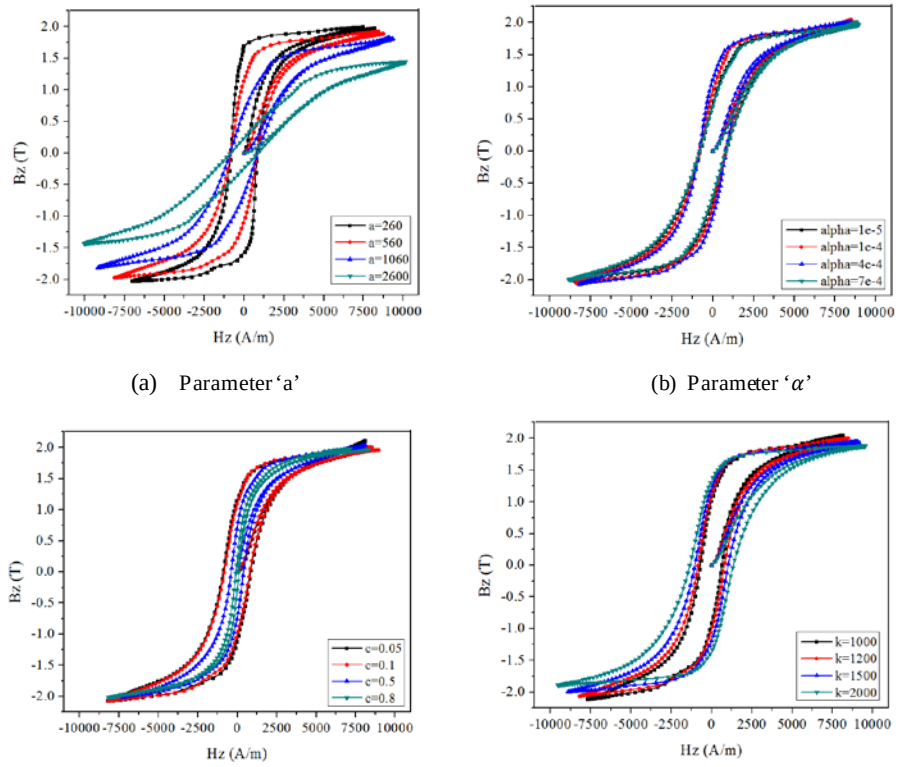

(a) Parameter 'a' (b) Parameter 'α'

(c) Parameter 'c' (d) Parameter 'k'

Fig. 6 Parametric study for parameters of inverse J-A hysteresis model

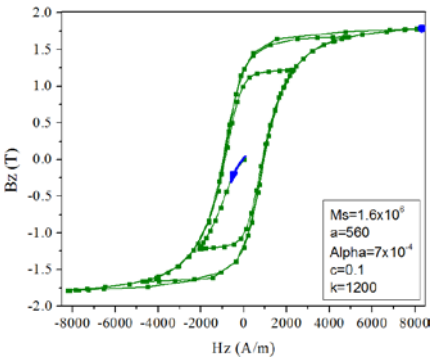

Fig 7. Simulated Bz-Hz loop result

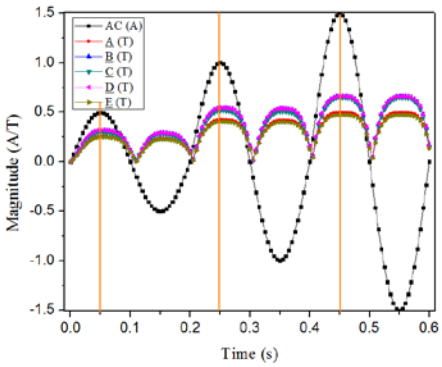

Fig 8. Alternating current and magnetic flux density

3.2 Temperature field

3.2.1 Core loss

Accurate power-loss estimation is essential in order to understand the distribution of temperature inside the MR damper, especially the fluid region, i.e. thermal effect on the characteristics of MR fluid. The core loss consists of: (i) the eddy current generated by a time varying magnetic field and (ii) hysteresis effect of the magnetic material. Inductive heating is essentially resistive heating ($I_e^2 R$) of the eddy current occurring inside the piston or external casing of cylinder. The differential form of the energy conservation law using Gauss's theorem can be given by

$$\rho C_p \frac{\partial T}{\partial t} - \nabla \cdot k\nabla \mathrm{T} = Q_{cl} \qquad (6)$$

The heat source Q_{cl} is separated into two parts: the eddy current Q_{em} and the hysteresis loss Q_{hl}. In the case of a harmonic electromagnetic loading, the heat source term Q_{em} can be written as,

$$Q_{em} = \frac{1}{2\sigma}|J_e|^2 \qquad (7)$$

where J_e is the induced current density in the

piston or casing calculated as $J_e = -i\omega\sigma A_\varphi$,

On the other hand, the hysteresis loss results from the ***B-H*** characteristic of ferro-magnetic materials following a different path for decreasing values of ***H*** than for increasing values of ***H***. The ***B-H*** characteristic becomes a hysteresis loop when H is carried through a complete cycle from $+H_{max}$ to $-H_{max}$ and back to $+H_{max}$. Moreover, the area of the magnetic hysteresis loop is proportional to the dissipation of waste energy in the form of heat due to magnetic hysteresis. Thus, for a piston or casing of cylinder having a uniform flux density B throughout the entire volume and varies cyclically from positive to negative values of B at a frequency of f, the hysteresis loss can be expressed empirically as

$$Q_{hl} = k_h f B_{max}^n \quad (8)$$

where the coefficient k_h depends on the material and n knows as Steinmetz exponent may varies from 1.5 to 2.5.

To investigate the thermal effect of MR damper due to the inductive heating and hysteresis loss dissipation, the equations (1)-(8) are solved based on the finite element analysis. For different constant current intensities $I_0 = 0.5, 1, 1.5, 2[A]$, the model simulation is performed with a coefficient $k_h = 0.2$, constant exponent $n = 1.8$, a frequency $f = 50[Hz]$ and a time-step $\Delta t = 1 \cdot 10^{-2}[s]$. It is apparent from figure 9 that the average temperature of MR fluid along the surface of piston due to the core loss rises as the current intensity increases. Within 600 milliseconds, average temperature of the MR fluid along the surface of the piston increases $0.05[K]$ by applying each of the four coils with current $I_0 = 0.5[A]$. However, when four coils are applied with current $I_0 = 2[A]$ respectively, the average temperature increment of the MR fluid along the piston jumps $0.68[K]$, as indicated in figure 10(a). Please note that when the damper is at rest, the heat generated by core less is transferred by conduction only. Therefore, when the velocity of the piston increases from 0 (static) to 3 [m/s], within 600 milliseconds the average temperature of the MR fluid along the piston can increase 0.08, 0.2, 0.58, 1.2[K] respectively. Further investigation indicates that temperature field behaves inhomogeneous distribution in the diametrical direction as indicated in figure 10(b). This is because that the temperature rise of the piston and cylinder is much faster than that of the cylinder over a period of time since the thermal conductivity of MR fluid (about $0.24[W/(m \cdot K)]$) is much smaller than that of ferro-magnetic steel (about $44.5[W/(m \cdot K)]$). On the other hand, the temperature variation of MR fluid changes its apparent viscosity (eq.11), namely the flow characteristics. In the applications of high power or high shear rate up to 1000 [s^{-1}] situations, the thermal effect exacerbates the shear thinning behaviors of MR fluids, thus affecting the performance of MR absorber. Thus the thermal effect on the MR fluid should also be considered under impact loading though the total processing time is less than 600 milliseconds.

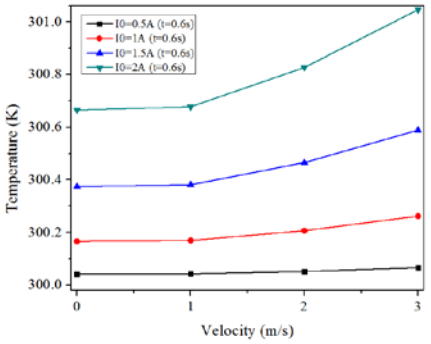

Fig 9. Average temperature of MR fluid along the surface of piston with increasing velocity

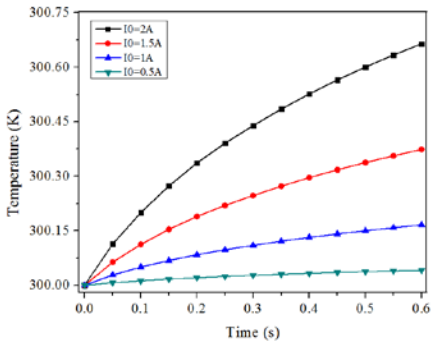

(a) Average temperature of MR fluid along the surface of piston

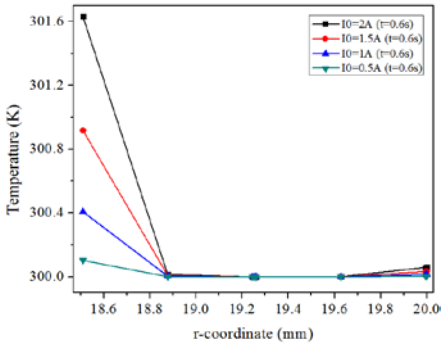

(b) Radial distribution of temperature (z=215mm)

Fig 10. Temperature in the MR fluid region

3.2.2 Conjugate heat transfer

As the piston head moves back and forth inside the damper cylinder, the MR fluid is forced to pass through the annular channel with large shear rate, which results in significant heat generation. The heat is transferred in both the fluid region and solid region, between which the temperature field is continuous. Conjugate heat transfer is utilized to describe the situation where the solid is dominated by conduction and the fluid is usually dominated by convection. In most cases, the heat transfer in solids can be described by Fourier's law defining the conductive heat flux (q) which is proportional to the temperature gradient $q = -k\nabla T$.

For a time-dependent problem, the temperature field in an immobile solid verifies the following form of the heat equation:

$$\rho C_p \frac{\partial T}{\partial t} = \nabla \cdot (k\nabla T) + Q_c \qquad (9)$$

where Q_c is the external heat source generated by the resistive heating of the exciting current (i^2R) applied on the electromagnetic coils.

Due to the MR fluid motion, four contributions should be included to the heat equation:

1: The flow of the fluid implies the energy transport as well, which appears in the heat equation as the convective contribution. In other words, either the convective or the conductive heat transfer can dominate, depending on the thermal properties of the fluid and the flow regime.

2: The fluid heating produced by the viscous effects of the fluid flow usually can neglected, nevertheless, its contribution is noticeable for fast flow in viscous fluids.

3: A pressure work term contributes to the heat equation as well, especially for the situation where large pressure is produced in a short time, for example, impact loading.

4: The heat generated by the core loss (section 2.2.1) also contributes to the heat equation as an external heat source.

Accounting for these contributions, in addition to the conduction, the following transient heat equation for the temperature field in a fluid can be concluded as:

$$\rho C_p \frac{\partial T}{\partial t} + \rho C_p \boldsymbol{u} \cdot \nabla T = \nabla \cdot (k\nabla T) + Q_t + Q_{vh} + W_p \qquad (10)$$

Please note that the temperature field and the heat flux are continuous at the fluid/solid interface. However, the temperature field may rapidly vary in a fluid due to the motion, which means that close to the solid, the fluid temperature is close to the solid temperature and far from the interface, the fluid temperature is close to the ambient fluid temperature.

3.3 Fluid dynamics

Before proceeding with the formulation and implementation of the coupled model, it seems necessary to summarize the different field

equations that govern the physical behaviors (Table 2). The link between above fields is given in simple terms by the dependence on the magnetic flux density $\boldsymbol{B}$ and the temperature T of the apparent viscosity η and the magnetic force f_m.

However, the description of the non-uniform yield stress in Bingham plastic model (or Herschel-Bulkley plastic model) leads to complications in computation due to its non-differentiability in the un-yielded regions of the MR fluid. One approach to the non-differentiability problem is to first determine the bounds of the un-yielded regions then to treat them as "plug flow" (a region in which the velocity is a constant vector). This approach, however, assumes fully developed flow and becomes far more complicated when dealing with complex channel geometries [28]. Another approach used in the study employs a commercial finite element software package and follows a close approximation of the Bingham plastic behavior, proposed by David Case *et al* [29]. Considering the temperature effect on the performance of the MR fluid, the viscosity gradually declines as the temperature rises within -40~100[℃] and after the temperature exceeds 100[℃] , the change of viscosity becomes irregular, which leads to unstable damping performance [30]. Indeed, the fluid viscosity is significantly a function of the composition and chemistry of the carrier oils. Therefore, in the absence of the external magnetic field, MR fluid exhibits Newtonian fluid-like behavior and only temperature influences its apparent viscosity . In the presence of the external magnetic field, the apparent viscosity of MR fluid under shearing flow model can be described through modified Bingham plastic model,

$$\eta(T) = [\eta_{T_0} + \frac{\tau_y \tanh(\zeta\dot{\gamma})}{\sqrt{\xi^2+\dot{\gamma}^2}}]e^{-\lambda(T-T_0)} \quad (11)$$

One may note that, the MR fluid is modeled in the typical manner for non-Newtonian fluids with variable viscosity which takes temperature effect into consideration. In such a way that the non-differentiability problem can be transferred to a close approximation of nonlinear multi-physics interaction process.

For a suspension of non-interacting spherical particles, the dipole interactions allow the formation of particle columns and the increase of the viscosity. It is important to deliberate the magnetic force, so that we can understand the physical mechanisms governing the dynamics of MR particles. Under an inhomogeneous magnetic field, the magnetic force f_m on the dipole is determined by

$$f_m = \mu_0 \boldsymbol{M} \cdot \nabla \boldsymbol{H} \quad (12)$$

where μ_0 is the permeability of free space, $\boldsymbol{M}$ is the magnetization vector, and $\boldsymbol{H}$ is the applied field vector. The volumetric magnetic susceptibility χ is the ratio of magnetization vector $\boldsymbol{M}$ to the applied field vector $\boldsymbol{H}$. The Maxwell-Garnett equation for magnetic susceptibility of a suspension of non-interacting spherical particles has the following form [31]

$$\chi = 3\varphi\chi_p/[3+\chi_p(1-\varphi)] \quad (13)$$

However, for dilute suspensions with low number φ, the equation (13) can be further transformed to the linear form [31]

$$\chi = (0.668D_p + 0.961)\varphi \quad (14)$$

where χ_p is the susceptibility of the particles, D_p is the particle diameter and φ is the volume fraction of the particles. By substituting for $\boldsymbol{M}$, using the vector identity,

$$H \cdot \nabla H = \nabla H \cdot \frac{H}{2} - H \times \nabla \times H \quad (15)$$

And noting the Ampere's law cancels out the curl of the applied field ($\nabla \times H = 0$), equation (12) can be reduced to

$$f_m = \mu_0 \chi \nabla \boldsymbol{H^2}/2 \quad (16)$$

Using the constitutive relation (relation between magnetic flux density and magnetic field vector), the magnetic induction vector in

the form can be written as

$$B = \mu_0(1+\chi)H \quad (17)$$

The finite element software COMSOL solves for a magnetic vector potential, $\boldsymbol{A}$, such that the magnetic flux density can also be defined as the curl of the magnetic vector potential ($\nabla \times \boldsymbol{A} = \boldsymbol{B}$). For the axisymmetric 2-D dimensions, $\boldsymbol{A}$ only has a φ-component, thus its curl can be written in index notation as,

$$\nabla \times \boldsymbol{A} = \begin{pmatrix} -\frac{\partial A_\varphi}{\partial z} \\ 0 \\ \frac{A_\varphi}{r} + \frac{\partial A_\varphi}{\partial r} \end{pmatrix} \quad (18)$$

From the above equations (12)-(18), the magnetic force f_m can be expressed by

$$f_m = \frac{\chi}{\mu_0(1+\chi)^2} \begin{pmatrix} \frac{\partial A_\varphi}{\partial z}\frac{\partial}{\partial r}\left(\frac{\partial A_\varphi}{\partial z}\right) + \left(\frac{A_\varphi}{r} + \frac{\partial A_\varphi}{\partial r}\right)\left(\frac{1}{r}\frac{\partial A_\varphi}{\partial r} - \frac{A_\varphi}{r^2} + \frac{\partial}{\partial r}\left(\frac{\partial A_\varphi}{\partial r}\right)\right) \\ 0 \\ \frac{\partial A_\varphi}{\partial z}\frac{\partial}{\partial z}\left(\frac{\partial A_\varphi}{\partial z}\right) + \left(\frac{A_\varphi}{r} + \frac{\partial A_\varphi}{\partial r}\right)\left(\frac{1}{r}\frac{\partial A_\varphi}{\partial z} + \frac{\partial}{\partial z}\left(\frac{\partial A_\varphi}{\partial r}\right)\right) \end{pmatrix} \quad (19)$$

This multi-physics FE model is becoming increasingly sophisticated since it couples complex interacting fields such as electromagnetics, heat transfer and fluid dynamics as listed in table 2. However, by including the coupling effects between different physics fields, the analyses are believed to provide a deeper insight into the behaviors of a MR absorber under constant current, sinusoidal excitations and impact loading, etc. Mathematically, the performance of the MR absorber are described by a set of coupled partial differential equations (PDFs). The solutions of these equations can be obtained regarding the robustness of the algorithmic solvers to handle such interactions in a general and efficient manner. The multi-physic analysis is primarily a finite element analysis approach with considerations of several aspects in the process, i.e. electromagnetics, heat transfer and fluid dynamics. All these aspects have been considered by introducing perspective PDFs in the finite element analysis. With this in mind, the apparent viscosity of the MR fluid $\eta(\dot{\gamma}, \boldsymbol{H}(\boldsymbol{B}), T)$ can be described as a function of the shear rate $\dot{\gamma}$, magnetic effect $\boldsymbol{H}(\boldsymbol{B})$ and the temperature T as shown in equation 11. In addition, the magnetic force f_m on the MR particles can be included as body force acting on a fluid element. The core loss generated by the eddy current and hysteresis loss is also included as an external heat source applying on the boundary conditions of the MR fluid flow. Finally, the multi-physics problem was analyzed by solving the Navier-Stokes equations which takes these coupling effects into account.

Table 2 Field equations

Electro-Magnetic Equations (Maxwell)	Conjugate Heat Transfer	Fluid Dynamic Equations (Navier-Stokes)
$\nabla \cdot \boldsymbol{E} = \frac{\rho_c}{\varepsilon_0}$ (Gauss Law)	$\rho C_p \frac{\partial T}{\partial t} + \rho C_p \boldsymbol{u} \cdot \nabla T = \nabla \cdot (k \nabla T) + Q_t + Q_{vh} + W_p$ (Heat Transfer in fluid)	$\frac{\partial \rho}{\partial t} + \nabla \cdot (\rho \boldsymbol{u}) = 0$ (Continuity)
$\nabla \cdot \boldsymbol{B} = 0$ (Gauss Law for Magnetism)	$Q_{vh} = \tau : S$ $S = \frac{1}{2}(\nabla \boldsymbol{u} + (\nabla \boldsymbol{u})^T)$ (Viscous heating)	$\rho \frac{\partial \boldsymbol{u}}{\partial t} + \rho \boldsymbol{u} \cdot \nabla \boldsymbol{u} = -\nabla p + \nabla \cdot \{\eta(\dot{\gamma}, H(B), T)(\nabla \boldsymbol{u} + (\nabla \boldsymbol{u})^T - \frac{2}{3}(\nabla \boldsymbol{u}) I)\} + f_m$ (Momentum) Viscosity Interaction Force Interaction
$\nabla \cdot \boldsymbol{E} = -\frac{\partial \boldsymbol{B}}{\partial t}$ (Faraday Induction Law)	$W_p = -\frac{T}{\rho}\frac{\partial \rho}{\partial T}\left(\frac{\partial \rho}{\partial t} + (\boldsymbol{u} \cdot \nabla) p\right)$ (Pressure work)	Constitutive equation (modified Bingham model) $\eta(\dot{\gamma}, H(B), T) = [\eta_{T_0} + \frac{\tau_y \tanh(\zeta \dot{\gamma})}{\sqrt{\xi^2 + \dot{\gamma}^2}}] e^{-\lambda(T - T_0)}$
$\nabla \times \boldsymbol{B} = \mu_0 \boldsymbol{J} + \mu_0 \varepsilon_0 \frac{\partial \boldsymbol{E}}{\partial t}$ (Ampere Circuital Law)	$Q_t = Q_{em} + Q_{hl} + Q_c$ (total external heat source)	Body force $f_m = \mu_0 \chi \nabla \boldsymbol{H}^2/2$

where $\boldsymbol{E}$=Electric field, [V/m]; $\boldsymbol{B}$=Magnetic field density, [T]; $\boldsymbol{H}$=Magnetic field strength, [A/m]; J=Current density, [A/$\mathbf{m^2}$]; $\boldsymbol{\rho_c}$=Volumetric charge density, [C/$\mathbf{m^3}$]; $\boldsymbol{\varepsilon_0}$=Permittivity of free space =8.85× $\mathbf{10^{-12}}$,[F/m]; $\boldsymbol{\mu_0}$=Permeability of free space =4$\boldsymbol{\pi}$ × $\mathbf{10^{-7}}$,[N/$\boldsymbol{A^2}$].	where C_p=specific heat capacity, [J/(kgK)]; T=absolute temperature, [K]; τ=viscous stress tensor, [Pa]; S=strain-rate tensor, [1/s]; Q=heat source, [W/m^3]. k=thermal conductivity, [W/(m·K)]	where $\boldsymbol{u}$=Velocity field, [m/s]; ρ=Fluid density, [kg/m^3]; $\dot{\gamma}$=Shear strain rate, [1/s]; η=Apparent viscosity , [Pa*s]; η_{T_0}=Apparent viscosity when no magnetic field is present at temperature T_0; p=Pressure in the fluid region, [Pa]; τ_y=Yield stress, [Pa]; ξ=small constant; ζ=scaling coefficient; λ= oil viscosity-temperature coefficient. χ= volumetric magnetic susceptibility

4. Multi-physics simulation with Inverse J-A hysteresis model

As explained before, the MR absorber includes the MR fluids and ferro-magnetic materials to form the magnetic flux path for a magnetic circuit. Thus the hysteresis behavior introduced in the current-force of the MR absorber results in such known problems in the control systems as tracking errors, limit cycles, and undesired stick-slip motions. To capture a precise nonlinear damper behavior subjected to varying current intensity, it is necessary to simulate by making the relevant multi-physic fields interact during the same time step.

As shown earlier, the MR absorber has a rotational periodicity, thus the axisymmetric 2-D dimension is considered to simplify the finite element model. The model was meshed by controlling the element size, and consists of free triangular elements; the total number of elements is 83,048 and the average element quality is 0.9784. Please note that the fluid region was adaptively meshed, since it needs much smaller element size to obtain an accurate velocity profile for the fluid. The boundary conditions applied to the model are corresponding to: (i) no-slip for the fluids at the inner cylinder and piston walls; (ii) an inlet at the initial end and an opening at the end of the fluid region with a relative pressure; and (iii) the yield-stress field obtained from the magnetic field that controls the fluid viscosity and magnetic force. Consequently, laminar flow is considered in the model and the specified constant velocity is $V_0 = 2[m/s]$ at the inlet. A transient multi-physics analysis is performed with a frequency of $f = 5[Hz]$, and a time step of $\Delta t = 5 \cdot 10^{-4}[s]$. This time step is selected as a reasonable comprise to obtain a better trade-off between accuracy and computation time.

Figure 11 shows the transient influence of magnetic field intensity generated by alternating exciting current i (equation (5)) on the magnetic flux density, velocity and pressure of MR fluid. Please note that the measure point was located in the center of annular gap (point C). The magnetic flux density $\boldsymbol{B}$ of the fluid region obtains 0.3, 0.52, 0.65[T] respectively as the magnitude of exciting current i increases from $0.5[A]$ to $1.5[A]$. Consequently, the fluid velocity in the measured point shows an opposite oscillation with the magnetic flux density. The maximum velocity and pressure drop due to MR effect reaches 1[m/s] and 2.2[MPa] in the 'active' fluid gap. However, when the hysteresis due to the ferro-magnetic materials is taken into account, the time lag between exciting current i and the magnetic flux density $\boldsymbol{B}$ ascends to $1\sim3$[ms]. Therefore, both the fluid velocity and pressure drop lags behind the varying of the exciting current i. This phenomenon can further be explained by the transient variation of fluid apparent viscosity as shown in figure 12. When exposed to a magnetic field, the magnetic particles move and form chains or linear structures, increasing the apparent viscosity of the fluid. In this way, the MR fluid changes from free-flowing liquid to a semi-solid with

yield stress, which acts as semi-active 'lock' to control the fluid velocity as well as pressure. Therefore, the transient variation of apparent viscosity in the 'active' area tends to dominate the fluid velocity and pressure, as shown in figure 12 (a). On the other hand, the velocity profile (or pressure drop) is still affected by the transient apparent viscosity with the remnant magnetic flux density, as indicated in figure 12 (b). So the output damping force of MR absorber always lags behind the input exiting current.

In addition, figure 13 shows the current-force curves to compare the results of those without hysteresis and those of inverse Jiles-Atherton predications. Obviously, the response of the damping force lags behind the exciting current due to the hysteresis of ferro-magnetic material. In addition to the different trajectories, the amplitude of the damping force is smaller compared to the case without hysteresis. This might be caused by the rise of the temperature inside the fluid gap. As shown in figure 14, the temperature of MR fluid tested at r=19.25mm, z=132.5mm goes up significantly with the increment of input velocity. Also the increased exciting current accelerates the increasing rate of temperature rising. Thus the apparent viscosity of the MR fluid shows decreasing trend with increasing temperature.

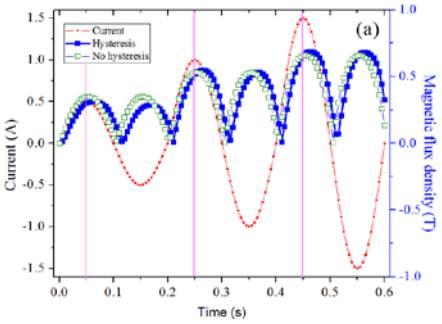

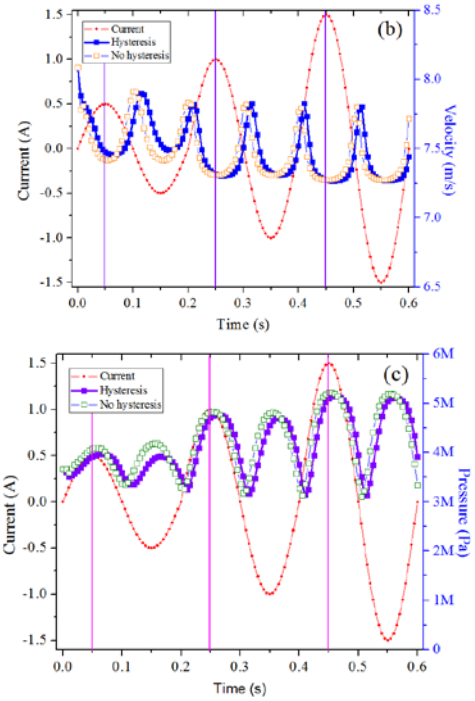

Fig 11 Effects of hysteresis on (a) magnetic flux density, (b) fluid velocity and (c) pressure (Measure point: C)

5. Impulse of MR absorber with step exciting current

This section investigates the response of the MR absorber under impact load with step exciting current based on the proposed inverse J-A hysteresis model. The impulsive tests were performed by installing the multi-coil MR absorber shown in figure 2 to an impact test system [21]. During the impact tests, the explosion of powder in the closed chamber produces a large impulsive force, under which the recoil mass together with the MR absorber cylinder moves along the guide rail. The recoil force was measured by a piezoelectric force transducer (Kistler 9351B) with a charger amplifier (Kistler 5011B). The recoil displacement and velocity were both measured by a magnetostrictive position sensor (RP profile-style position sensor). The above output signals were both acquired and displayed by a dSPACE real time system.

A typical impact force caused by gunpowder can be identified as two phases

[33, 34]. However, due to external influences (humidity, temperature, burning rate, etc), the impact force becomes highly nonlinear and unstable, resulting in the difficulty of normalizing. To simplify the expression caused by the impact load, the output velocity $\tilde{V}$ based on the experimental data were normalized versus the time as shown in figure 15. The output velocity of the recoil (piston) caused by gunpowder is characterized as three phases. In the first phase, the gunpowder experiences a very short period of time during its explosion in the closed chamber; here $\tilde{V}$ is mainly determined by the average pressure inside the closed chamber, though the recoil movement starts to be resisted by increasing damping force. The second phase (transition phase) is at the end of the period of the effects caused by the gunpowder gas. This period experiences a sharp fall of the gas pressure and density in the chamber and therefore a balance point between the impact force and damping force, thus a maximum velocity is reached in this period. The third phase starts at the moment when the contact mass separates from the recoil mass. After the separation, the recoil mass can be regarded as free damping movement with an initial velocity until completely stop.

In simulation of the output velocity from the explosion of gunpowder, $\tilde{V}$ can be fitted as a combination of exponential forms.

$$\tilde{V} = \begin{cases} \sum_{i=0}^{n} \tilde{a}_i' e^{(-((t-\tilde{b}_i')/\tilde{c}_i')^2)} & (Phase1: 0 < t \le \tilde{t}_s) \\ \sum_{j=0}^{n} \tilde{a}_j'' e^{(-((t-\tilde{b}_j'')/\tilde{c}_j'')^2)} - (\tilde{\alpha} I^{\tilde{\beta}} + \tilde{\gamma}) e^{\tilde{\theta} t} & (Phase2: \tilde{t}_s < t \le \tilde{t}_p) \\ \sum_{k=0}^{w} \tilde{a}_k''' e^{(-((t-\tilde{b}_k''')/\tilde{c}_k''')^2)} - (\tilde{\alpha} I^{\tilde{\beta}} + \tilde{\gamma}) e^{\tilde{\theta} t} & (Phase3: \tilde{t}_p < t \le \tilde{t}_e) \end{cases} \quad (20)$$

The fitting parameters are given in table 3. Please note that the impact force dominates the movement of the recoil mass and the damping force produced by the MR absorber is very small compared to the impact load in the first phase period.

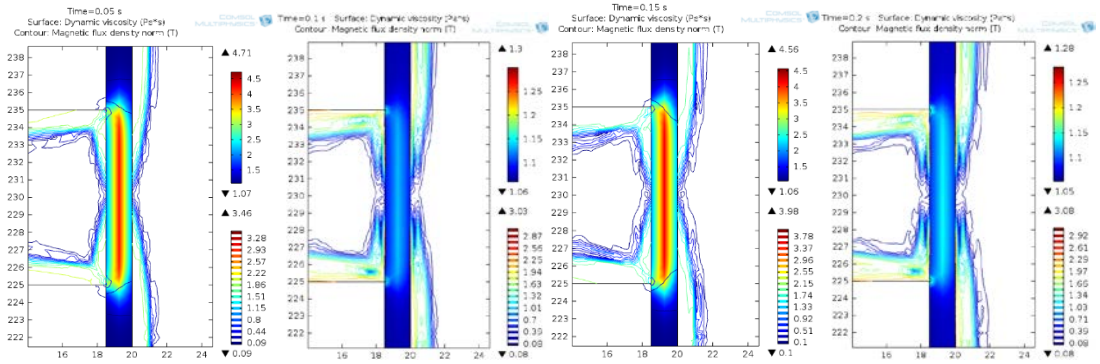

(a) Without hysteresis model

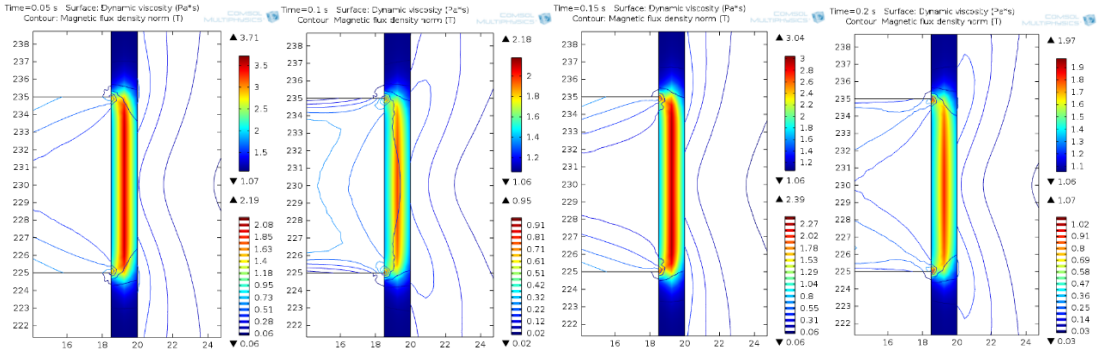

(b) With inverse J-A model

Fig 12 Transient variation of fluid apparent viscosity (display domain: center of annular gap)

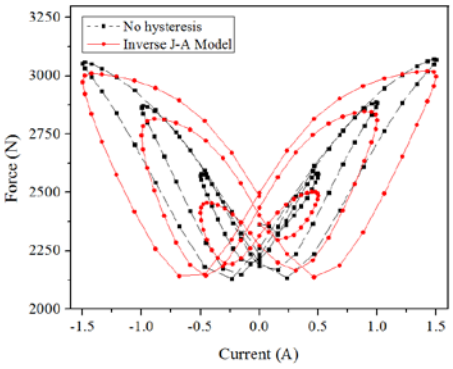

Fig 13 Current-force diagram

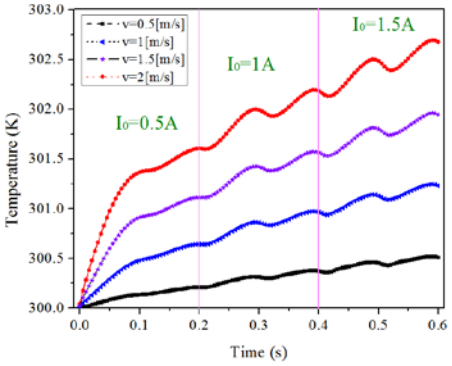

Fig 14 Temperature of MR fluid (measured point: E)

Table 3 Simulation parameters of output velocity $\tilde{V}$

$\tilde{a}_1'$	3.531	$\tilde{b}_1''$	0.05865	$\tilde{t}_p$	0.075	$\tilde{b}_3'''$	0.1025	m	2
$\tilde{b}_1'$	0.05763	$\tilde{c}_1''$	0.008337	$\tilde{a}_1'''$	0.7347	$\tilde{c}_3'''$	0.0126	n	3
$\tilde{c}_1'$	0.02843	$\tilde{a}_2''$	3.473	$\tilde{b}_1'''$	0.06103	$\tilde{a}_4'''$	0.104	w	5
$\tilde{a}_2'$	1.706	$\tilde{b}_2''$	0.04231	$\tilde{c}_1'''$	0.007408	$\tilde{b}_4'''$	0.13	$\tilde{t}_e$	0.2
$\tilde{b}_2'$	0.02614	$\tilde{c}_2''$	0.04712	$\tilde{a}_2'''$	0.293	$\tilde{c}_4'''$	0.006964	$\tilde{\alpha}$	0.1751
$\tilde{c}_2'$	0.01778	$\tilde{a}_3''$	0.735	$\tilde{b}_2'''$	0.08089	$\tilde{a}_5'''$	3.297	$\tilde{\beta}$	0.8265
$\tilde{t}_s$	0.039	$\tilde{b}_3''$	0.07437	$\tilde{c}_2'''$	0.01039	$\tilde{b}_5'''$	-0.05263	$\tilde{\gamma}$	0.32
$\tilde{a}_1''$	0.5184	$\tilde{c}_3''$	0.007093	$\tilde{a}_3'''$	0.1794	$\tilde{c}_5'''$	0.3224	$\tilde{\theta}$	3.474

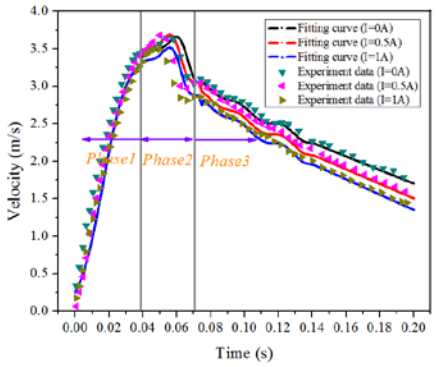

Fig 15 Three phases of fitting velocity

A group of impact tests were performed on the real-scale MR absorber with different constant current intensities $I_0 = 0, 0.5$ and $1[A]$ respectively. Figure 16 shows the step response of magnetic flux density which is measured in the MR fluid gap at r=19.25mm, z=132.5mm. t_p is defined as the required time to set up the constant current density due to external current driver or controller. It is apparent from the Figure 16 that as it was expected, the response of the magnetic field lags behind the step exciting current due to the inherent hysteresis of ferro-magnetic materials. As explained in section 3.2.1, the thermal effect on the MR fluid can't be ignored under high velocity even in a short time. In fact, as presented in Figure 17, the field-off temperature of the MR fluid can increase 1.6[K] within 70 milliseconds under input velocity $\tilde{V}$ with peak value of 3.5[m/s]. However, the maximum temperature increases 2.3 and 2.5[K] when the electromagnetic coils are applied with 0.5 and 1[A] respectively. Obviously, the temperature of MR fluid decreases with the decreasing velocity of recoil mass, which indicates that the velocity plays a major role in controlling the temperature of MR fluid.

Finally, shown in Figure 18 is the history of damping force measured during the impact tests by the input velocity $\tilde{V}$ with constant current density $I_0 = 0, 0.5$ and $1[A]$ respectively. The numerical results almost agree well with the experimental data though some peak values can't be fully captured. This is because that some external factors, for

example, friction and turbulent flow, etc, may result in the protuberance of the damping force. Obviously, it can more precisely describe the history of the damping force by taking the inherent hysteresis of ferro-magnetic materials into account. Furthermore, it is apparent from figure 18 that the damping force shows a 'delayed' response in the beginning of first phase. This is because there exists a certain volume of air bubble inside the chamber of MR absorber, which results in the compressibility of air bubble. However, this phenomenon wasn't considered in the FEA simulation due to the uncertainty of each test. One way to eliminate this phenomenon is the design and fabrication of a new MR absorber with compensation, which will be the future work. Although somewhat error may be existed between the results of the numerical simulation and real measured data, the inverse Jiles-Atherton model can also be adopted as a potential candidate for capturing the transient hysteresis characteristics of MR devices. On the other hand, the somewhat error can be somehow minimized by increasing the accuracy of the FEA simulation. However, this implies significant growing in number of data and consequently increasing the computation time and the capacity of required memory to store the data.

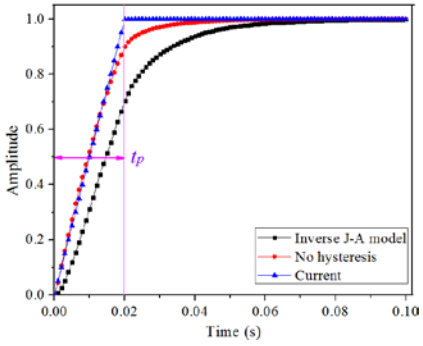

Fig 16 step response of magnetic flux density in the fluid gap

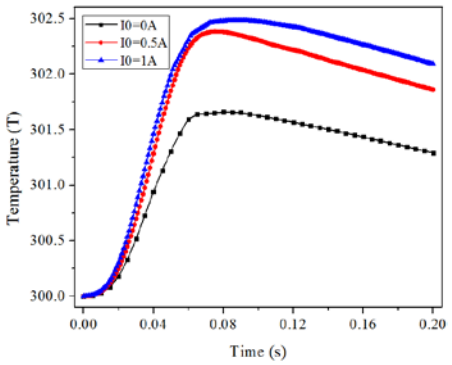

Fig 17 Temperature of MR fluid under impact loading (measured point: E)

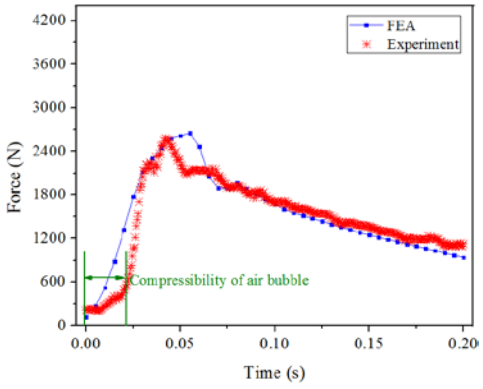

(a) 'off-field'

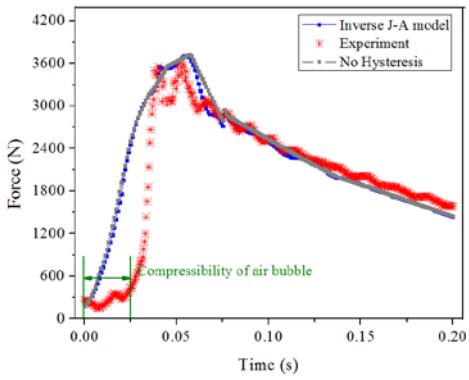

(b) I_0=0.5A

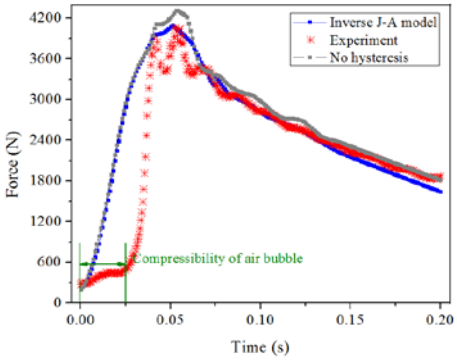

(c) I_0=1A

Fig 18 Damping force under impact loading

6. Conclusion

In this paper, a multi-physics FEM model with hysteresis phenomenon is proposed to study the dynamic characteristics of a MR absorber. It can be stated that such a model is a promising tool for designing a MR absorber in order to optimize its overall performance and save experimental time and costs. The results obtained in this work can be summarized as:

1. An inverse Jiles-Atherton hysteresis model was implemented into the magnetic field to fully capture the dynamic hysteresis behaviors of MR absorber. A parametric study of the J-A parameters were performed to better fit over the entire range of the hysteresis loop. The temperature field takes core loss (i.e. eddy current loss and hysteresis loss) and conjugate heat transfer into account. The numerical results show that the temperature of the MR fluid inside the annular gap gains $2.5\,[K]$ within 600ms by velocity $V_0 = 2[m/s]$ and currents $I_0 = 1.5[A]$.

2. Different field equations including electromagnetics, heat transfers and fluid dynamics were summarized to formulate the multi-physics FEM model. The current-force curve indicates that the damping force lags behind the exciting current and the amplitude of the damping force is weakened by the rise of temperature in the fluid gap.

3. The response of the MR absorber was investigated under impact loading with step exciting current based on the multi-physics FEM model. To simplify the expression caused by the impact load, the output velocity $\tilde{V}$ based on the experimental data were fitted as a combination of exponential forms. As it was expected, the response of the magnetic field lags behind the step exciting current and the high velocity dominates the variation of temperature in the fluid gap. The numerical results of damping force almost agree well with the experimental data though some peak values can't be fully captured. In the future research, a phenomenon like compressibility of air bubble might be added into the multi-physics FEA model.

ACKNOWLEGEMENTS

This work has been supported by a Natural Science Foundation of China (NSFC) grant funded by the Chinese government (No.51175265 and No.51305207). This work was also supported by China Scholarship Council (CSC, No.201306840019)

Reference

[1]. Kwok, N. M., Q. P. Ha, T. H. Nguyen, Jianchun Li, and Bijan Samali. A novel hysteretic model for magnetorheological fluid dampers and parameter identification using particle swarm optimization. Sensors and Actuators A: Physical 132, no. 2 (2006): 441-451.

[2]. Esteki, Kambiz, Ashutosh Bagchi, and Ramin Sedaghati. Dynamic analysis of electro-and magneto-rheological fluid dampers using duct flow models. Smart Materials and Structures 23, no. 3 (2014): 035016.

[3]. Spencer BF Jr, Dyke SJ, Sain MK, et al. (1997) Phenomenological model for magnetorheological dampers. Journal of Engineering Mechanics: ASCE 123(3): 230–238. [2] Lee, T.Y. and Kawashima, K. (2007). Semi-Active Control of Nonlinear Isolated Bridges with Time Delay. Journal of Structural Engineering, ASCE 133:2, 235-241.

[4]. Kamath GM and Wereley NM (1997). Non-linear visco-elastic-plastic mechanism-based model of an electrorheological damper. Journal of Guidance, Control and Dynamics 20(6): 1125–1132.

[5]. Wereley NM, Pang L and Kamath GM (1998). Idealized hysteresis modeling of electrorheological and magnetorheological dampers. Journal of Intelligent Material Systems and Structures 9(8): 642–649.

[6]. Zhou Q, Nielsen SRK and Qu WL (2006). Semi-active control of three-dimensional vibrations of an

inclined sag cable with magnetorheological dampers. Journal of Sound and Vibration 296(1): 1–22.

[7]. Choi SB, Lee SK and Park YP (2001). A hysteresis model for the field-dependent damping force of a magnetorheological damper. Journal of Sound Vibration 245(2): 375–383.

[8]. Ma XQ, Wang ER, Rakheja S, et al. (2002). Modeling hysteretic characteristics of MR fluid damper and model validation. In: Proceedings of the 41st IEEE conference on decision and control, vol. 2, Las Vegas, NV, 10–13 December, pp. 1675–1680. New York: IEEE.

[9]. Du H, Lam J and Zhang N (2006). Modelling of a magnetorheological damper by evolving radial basis function networks. Engineering Applications of Artificial Intelligence 19(8): 869–881.

[10]. Wang DH and Liao WH (2004). Modeling and control of magnetorheological fluid dampers using neural networks. Smart Materials and Structures 14(1): 111–126.

[11]. Wilson, Claudia Mara Dias, and Makola M. Abdullah. Structural vibration reduction using fuzzy control of magnetorheological dampers. Metropolis and Beyond. 2005.

[12]. Gordaninejad F and Wang X 2007 Flow analysis and modeling of field-controllable, electro- and magneto-rheological fluid dampers J. Appl. Mech. 74 13–22.

[13]. Wereley N M 2008 Nondimensional Hersche–Bulkley analysis of magnetorheological and electrorheological dampers J. Intell. Mater. Syst. Struct. 19 257–68.

[14]. Guo, Pengfei, Xinchun Guan, and Jinping Ou. Physical modeling and design method of the hysteretic behavior of magnetorheological dampers. Journal of Intelligent Material Systems and Structures (2013): 1045389X13500576.

[15]. An Jinung and Dong-Soo Kwon. Modeling of a magnetorheological actuator including magnetic hysteresis. Journal of Intelligent Material Systems and Structures 14.9 (2003): 541-550.

[16]. Rene Zemp, Juan Carlos de la Liera and Felix Weber, Experimental analysis of large capacity MR dampers with short- and long-stroke. Smart Mater. Struct. 23 (2014) 125028 (15pp).

[17]. Jedryczka, Cezary, Piotr Sujka, and Wojciech Szelag. The influence of magnetic hysteresis on magnetorheological fluid clutch operation. COMPEL-The international journal for computation and mathematics in electrical and electronic engineering 28.3 (2009): 711-721.

[18]. Erol, Ozan, Berk Gonenc, Doruk Senkal, Sait Alkan, and Hakan Gurocak. Magnetic induction control with embedded sensor for elimination of hysteresis in magnetorheological brakes. Journal of Intelligent Material Systems and Structures 23, no. 4 (2012): 427-440.

[19]. Alan Sternberg, René Zemp, and Juan Carlos de la Llera. Multiphysics behavior of a magneto-rheological damper and experimental validation. Engineering Structures 69 (2014): 194-205.

[20]. Zhu, Xiaocong, Xingjian Jing, and Li Cheng. Magnetorheological fluid dampers: A review on structure design and analysis. Journal of Intelligent Material Systems and Structures 23, no. 8 (2012): 839-873.

[21]. Zheng, Jiajia, Zhaochun Li, Jeong-Hoi Koo, and Jiong Wang. Analysis and compensation methods for time delays in an impact buffer system based on magnetorheological dampers. Journal of Intelligent Material Systems and Structures (2014): 1045389X14549868.

[22]. Sternberg, A., Zemp, R., & de la Llera, J. C. Multiphysics behavior of a magneto-rheological damper and experimental validation. Engineering Structures, 69, 194-205, 2014.

[23]. Gedik, E., Kurt, H., Recebli, Z., & Balan, C. Two-dimensional CFD simulation of magnetorheological fluid between two fixed parallel plates applied external magnetic field. Computers & Fluids, 63, 128-134, 2012.

[24]. Baghel, A. P. S., S. K. Shekhawat, S. V. Kulkarni, and I. Samajdar. Modeling of dynamic hysteresis for grain-oriented laminations using a viscosity-based modified dynamic Jiles–Atherton model. Physica B: Condensed Matter 448 (2014): 349-353.

[25]. Baghel, A. P. S., and S. V. Kulkarni. Dynamic Loss Inclusion in the Jiles–Atherton (JA) Hysteresis Model Using the Original JA Approach and the Field Separation Approach. Magnetics, IEEE Transactions on 50, no. 2 (2014): 369-372.

[26]. Rosenbaum, Sören, Michael Ruderman, Tom Strohla, and Torsten Bertram. Use of Jiles–Atherton and Preisach hysteresis models for inverse feed-forward control. Magnetics, IEEE Transactions on 46, no. 12 (2010): 3984-3989.

[27]. Sadowski, N., N. J. Batistela, J. P. A. Bastos, and M. Lajoie-Mazenc. An inverse Jiles-Atherton model to take into account hysteresis in time-stepping finite-element calculations. IEEE Transactions on Magnetics 38, no. 2 (2002): 797-800.

[28]. M. Moyers-Gonzalez and I. Frigaard, Numerical solution of duct flows of multiple visco-plastic fluids, Journal of Non-Newtonian Fluid Mechanics, vol. 122, pp. 227–241, 2004.

[29]. D. Case, B. Taheri, and E. Richer, Dynamical Modeling and Experimental Study of a Small-Scale Magnetorheologcial Damper, IEEE/ASME transactions on mechatronics, VOL. 19, NO. 3, June 2014.

[30]. Chen Song, Jin Huang, Kailin Jian and Jun Ding. Analysis of Influence of Temperature on Magnetorheological Fluid and Transmission Performance. Advances in Materials Science and Engineering (2014).

[31]. S R Gorodkin, R O James and W I Kordonski. Magnetic Properties of Carbonyl Iron particles in Magnetorheological Fluids. 11th Conference on Electrorheological Fluids and Magnetorheological Suspensions, Journal of Physics: Conference Series 149 (2009) 012051.

[32]. Zheng, Jiajia, Zhaochun Li, JeongHoi Koo, and Jiong Wang. Magnetic Circuit Design and Multiphysics Analysis of a Novel MR Damper for Applications under High Velocity. Advances in Mechanical Engineering 2014 (2014).

[33]. Li ZC and Wang J (2012) A gun recoil system employing a magnetorheological fluid damper. Smart Mater. Struct. 21 105003.

[34]. Wang Jiong, and Yancheng Li. Dynamic simulation and test verification of MR shock absorber under impact load. Journal of intelligent material systems and structures 17, no. 4 (2006): 309-314.

[35]. Meisami-Azad, Mona, Karolos M. Grigoriadis, and Gangbing Song. Anti-windup linear parameter varying control of structural systems with magneto-rheological dampers. Journal of Vibration and Control (2012): 1077546312451300.

Table 4 Material properties

Materials	Properties	
MRF 132DG	Fluid density	3006[kg/m^3]
	Dynamic viscosity @ 40℃	0.112 [Pa·s]
	Operating temperature	-40 ~+130 [℃]
	Heat capacity at constant pressure	2100[J/(kg·K)]
	Thermal conductivity	0.24[W/(m·K)]
	Electrical conductivity	5e-7[S/m]
	Relative permittivity	2.293
	Ratio of specific heats	1.34
	BH curve	Figure 19(a)
	Field dependent yield stress	Figure 19(b)
Silicon steel	Density	7850[kg/m^3]
	Heat capacity at constant pressure	475[J/(kg·K)]
	Thermal conductivity	44.5[W/(m·K)]
	Electrical conductivity	4.032e6[S/m]
	Magnetization curve	Inverse J-A model (Figure 7)
Copper	Density	8700[kg/m^3]
	Heat capacity at constant pressure	385[J/(kg·K)]
	Thermal conductivity	400[W/(m·K)]
	Electrical conductivity	5.998e7[S/m]
	Relative permeability	1

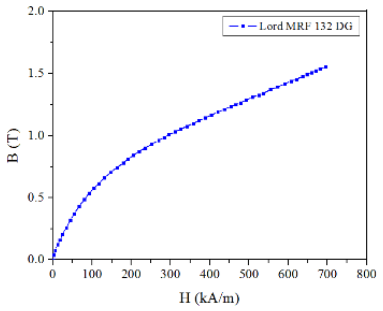

(a) BH curve

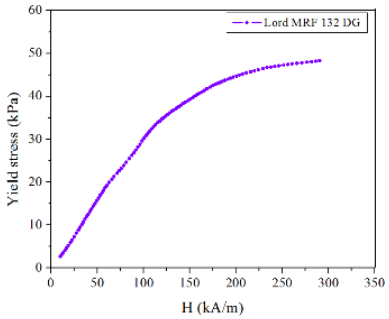

(b) Yield stress versus magnetic field strength

Fig. 19 Magnetic properties of MRF-132DG fluid

Appendix

Nomenclature			
A_φ	φ component of magnetic vector potential	T	Absolute temperature
$\boldsymbol{B}$	Magnetic flux density	T_0	Initial temperature (300 [K])
C_p	Heat capacity at constant pressure	$\boldsymbol{u}$	Velocity field of MR fluid

$\boldsymbol{E}$	Electric field	V_0	Constant input velocity
f	Frequency	$\tilde{V}$	Output velocity from experimental data
$\boldsymbol{H}$	Magnetic field strength	W_p	Pressure work
H_c	Coercivity	R	Resistance
$\boldsymbol{i}$	Alternating current (AC)	η	Apparent viscosity
I_{max}	Maximum value of alternating current	η_{T_0}	Apparent viscosity at temperature T_0
I_e	Eddy current	$\emptyset$	Magnetic flux
J	External current density	Θ_{inv}	Electromotive force (EMF)
J_φ	φ component of external current density	N	Turns of copper wire
J_e	Induced current density	ω	Angular frequency
k	Thermal conductivity	σ	Electric conductivity
k_h	Constant coefficient	μ	Magnetic permeability
$\boldsymbol{M}$	Magnetization	μ_0	Permeability of free space
M_s	Saturation magnetization	ε	Electric permittivity
M_{rev}	Reversible component of inverse J-A model	ε_0	Permittivity of free space
M_{irr}	Irreversible component of inverse J-A model	ρ	Density
M_{an}	Anhysteretic magnetization	ϑ	Skin depth
n	Steinmetz exponent	a, α, c, k	Parameters of inverse J-A model
p	Fluid pressure	δ	Directional parameter of inverse J-A model
q	Conductive heat flux	ϵ, ζ, λ	Coefficients of modified Bingham plastic model
Q_t	Total external heat source	τ_y	Yield Stress of MR fluid
Q_{em}	Heat source due to eddy current	χ	Volumetric magnetic susceptibility
Q_{hl}	Heat source due to hysteresis loss	χ_p	Susceptibility of MR particle
Q_c	Heat source due to applied exciting current	D_p	Particle diameter
Q_{vh}	Viscous heating	φ	Volume fraction of MR particle
r	r axis of cylindrical coordinate system	τ	Viscous stress tensor
z	z axis of cylindrical coordinate system	S	Strain rate tensor
t	Simulation time	$\dot{\gamma}$	Shear rate of fluid
Δt	Simulation time step	ρ	Density
t_p	Inductive time constant	f_m	Magnetic force